

UNIVERSITY OF CALIFORNIA  
Los Angeles

NO TITLE!?!?

A dissertation submitted in partial satisfaction  
of the requirements for the degree  
Doctor of Philosophy in Physics

by

Tyler Christopher Lam

2023

© Copyright by  
Tyler Christopher Lam  
2023

The dissertation of Tyler Christopher Lam is approved.

Michalis Bachtis, Committee Chair

University of California, Los Angeles

2023



## TABLE OF CONTENTS

<b>1 Experimental Apparatus . . . . .</b>	<b>1</b>
1.1 The Large Hadron Collider . . . . .	1
1.2 The Compact Muon Solenoid . . . . .	4
1.2.1 CMS Coordinate System . . . . .	5
1.2.2 Inner Tracker . . . . .	6
1.2.3 Electromagnetic Calorimeter . . . . .	8
1.2.4 Hadronic Calorimeter . . . . .	10
1.2.5 Muon Detectors . . . . .	12
1.2.6 Trigger System . . . . .	16
<b>References . . . . .</b>	<b>20</b>

## LIST OF FIGURES

1.1	LHC luminosity report. Left: breakdown of the CMS integrated luminosity by year from 2010-2022. Right: peak luminosity from 2016-2018 data taking [1]. . . . .	3
1.2	Diagram of the CERN accelerator complex during 2018 data taking. Protons begin as hydrogen atoms at Linac2 and collide at various detectors along the LHC at $\sqrt{s} = 13$ TeV . . . . .	3
1.3	Cutaway diagram of CMS showcasing major detector components [2]. . . . .	4
1.4	$r$ - $z$ slice of the CMS pixel detector [3] . . . . .	7
1.5	$r$ - $z$ slice of the CMS silicon detector, detailing the four main components of the strip detector [4] . . . . .	8
1.6	Geometry of the CMS ECAL showing the barrel, endcap, and preshower, adapted from [5] . . . . .	10
1.7	$r$ - $z$ slice of the CMS HCAL showing the HB, HE, HF, and HO [6] . . . . .	12
1.8	Diagram of the CMS Muon system [7] . . . . .	13
1.9	Diagram of the CMS Drift Tubes [8] . . . . .	14
1.10	Cut-away diagram of a single CSC module [9] . . . . .	15
1.11	Diagram of the double RPC at CMS [10] . . . . .	16
1.12	CMS Level-1 Trigger architecture during Run 2 [11] . . . . .	18

## LIST OF TABLES

## ACKNOWLEDGMENTS

## VITA

- 2015 Undergraduate Research Intern, SLAC National Accelerator Laboratory
- 2015-2017 Undergraduate Research Assistant, University of Virginia, Charlottesville, Virginia
- 2017 B.S (Physics) and B.A. (Mathematics), University of Virginia
- 2017-2018 Teaching Assistant, Department of Physics and Astronomy, UCLA, Los Angeles, California
- 2018 M.S. (Physics) UCLA
- 2018-2023 Graduate Research Assistant, Department of Physics and Astronomy, UCLA

# CHAPTER 1

## Experimental Apparatus

### 1.1 The Large Hadron Collider

The Large Hadron Collider (LHC) is a circular collider spanning the border between France and Switzerland, based at the European Organization for Nuclear Research (CERN). The central features of the LHC are the superconducting rings, located about 100 m underground with a circumference of 27 km, designed to collide counter-rotating beams of protons or heavy ions at highly relativistic energies. Along the rings lie four major experiments: ATLAS, CMS, ALICE, and LHCb. Both ATLAS and CMS are general purpose detectors, designed to probe a wide range of physics including the Higgs boson, precision measurements of fundamental constants, and physics beyond the standard model (BSM). The remaining two experiments are more specialized; ALICE measures quark gluon plasma produced in heavy ion collisions and LHCb focuses on  $b$ -quark physics and CP violation.

Two prominent aspects of the LHC are the high center of mass energy, referred to using the Mandelstam variable  $\sqrt{s}$ , and high instantaneous luminosity  $\mathcal{L}$ , often referred to as just luminosity. High  $\sqrt{s}$  allows for the production of more massive particles, giving more access to possible BSM physics, while high luminosity is essential for measuring rare processes and precision measurements. A process with cross section  $\sigma$  will have a rate  $R$  given by

$$R = \mathcal{L}\sigma \tag{1.1}$$

The cross section  $\sigma$  is a measure of how probable a process is to occur, and is in units of

area. They are frequently measured in barns, where  $1 \text{ b} = 100 \text{ fm}^2$ . Conversely, luminosity uses units of  $\text{Hz}/\text{b}$ . In cases where the relevant quantity is the total number of events, the integrated luminosity can be defined as  $\mathcal{L}_{\text{int}} = \int \mathcal{L} dt$  to give

$$N_{\text{events}} = \mathcal{L}_{\text{int}} \sigma \quad (1.2)$$

The luminosity depends on the characteristics of the proton beam and can be written in terms of the operational parameters of the detector given by

$$\mathcal{L} = \frac{N_b^2 n_b f_{\text{rev}} \gamma_r}{4\pi \epsilon_n \beta^*} F \quad (1.3)$$

where  $N_b$  is the number of particles per bunch,  $n_b$  is the number of bunches per ring,  $f_{\text{rev}}$  is the LHC revolution frequency,  $\gamma_r$  is the Lorentz factor for the proton,  $\epsilon_n$  is the transverse normalized beam emittance,  $\beta^*$  is the amplitude function at the collision point, and  $F$  is a geometric reduction factor based on the crossing angle of the two beams. The nominal design parameters of the LHC were intended to support a peak luminosity of  $12 \text{ Hz/nb}$  [12], but were exceeded by nearly twice that value of  $20.7 \text{ Hz/nb}$  during 2017 data taking and again with  $21.4 \text{ Hz/nb}$  in 2018. The LHC produced an integrated luminosity of  $41.6 \text{ fb}^{-1}$  in 2016,  $49.8 \text{ fb}^{-1}$  in 2017, and  $67.9 \text{ fb}^{-1}$  in 2018 for a total of  $159.3 \text{ fb}^{-1}$  during run 2 data taking. A more detailed breakdown of the LHC luminosity records can be seen in Fig. 1.1.

The protons used in collisions begin as hydrogen atoms, which are first ionized using electric fields to strip the electrons. They are first accelerated to  $50 \text{ MeV}$  through a linear accelerator Linac2 before entering the Proton Synchrotron Booster (PSB), where they will reach a kinetic energy of  $1.4 \text{ GeV}$ . Next, the protons are accelerated by the Proton Synchrotron (PS) and Super Proton Synchrotron (SPS), where they are accelerated to  $26 \text{ GeV}$  and  $450 \text{ GeV}$  respectively. Finally, the beams are injected into the LHC where they undergo acceleration to  $6.5 \text{ TeV}$ , producing the desired center of mass energy of  $\sqrt{s} = 13 \text{ TeV}$ .

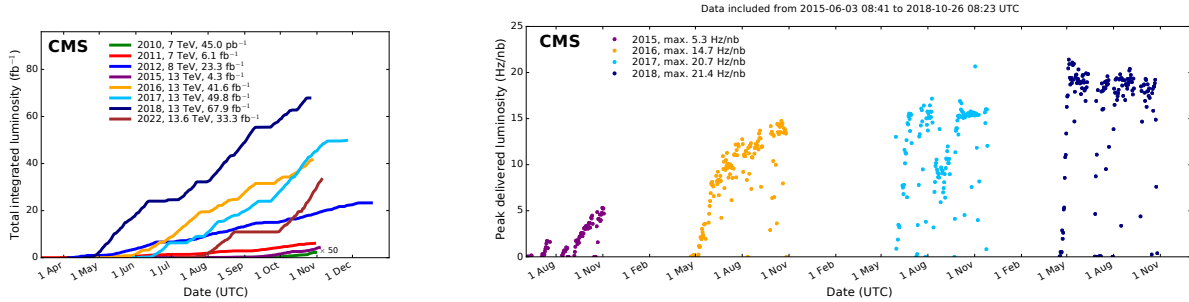


Figure 1.1: LHC luminosity report. Left: breakdown of the CMS integrated luminosity by year from 2010-2022. Right: peak instantaneous luminosity from 2016-2018 data taking [1]

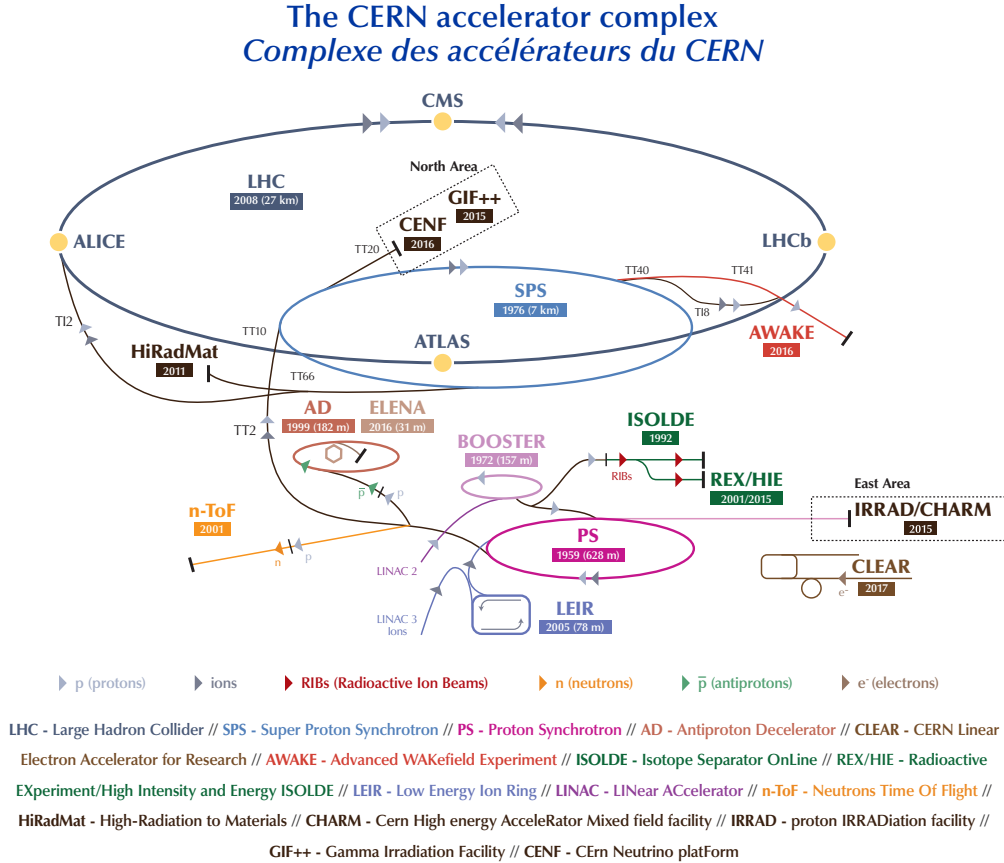


Figure 1.2: Diagram of the CERN accelerator complex during 2018 data taking [13]. Protons begin as hydrogen atoms at Linac2 and are accelerated in several stages to reach 6.5 TeV

## 1.2 The Compact Muon Solenoid

The Compact Muon Solenoid (CMS) is one of the two general purpose detectors at the LHC, designed to reconstruct physics events from proton-proton collisions. It is a cylindrical apparatus with its major axis aligned with the proton beams from the LHC, consisting of several concentric layers of specialized detectors. The innermost layer consists of a silicon tracker, followed by an electromagnetic and hadronic calorimeter (ECAL and HCAL, respectively). Surrounding those is the superconducting solenoid, which provides a 4 T magnetic field to bend the trajectory of charged particles. Lastly, layers of muon chambers are interspersed with an iron return yolk, designed to pull the magnetic field lines into the muon chambers.

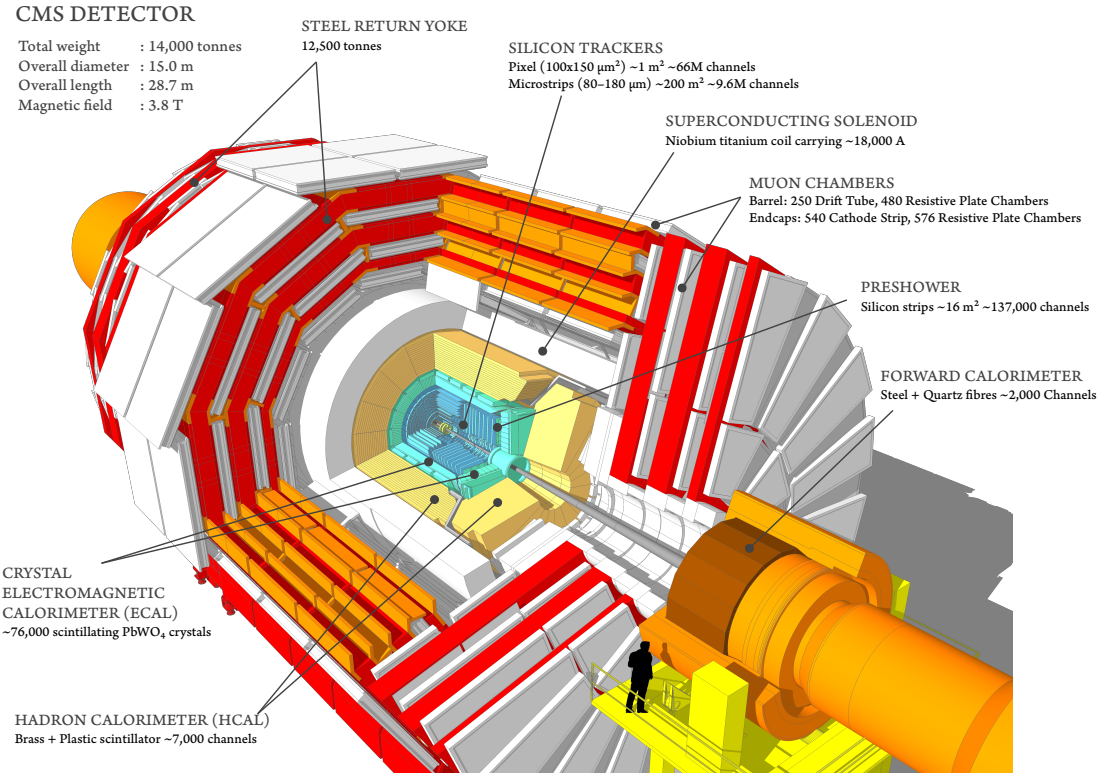


Figure 1.3: Cutaway diagram of CMS showcasing major detector components [2].

### 1.2.1 CMS Coordinate System

The origin of the CMS coordinate system is located at the center of the detector, at the nominal collision point of the proton beams. The  $+\hat{x}$  axis points radially towards the center of the LHC, while the  $+\hat{y}$  axis points vertically upward. This sets the  $+\hat{z}$  direction along the beamline, counterclockwise along the LHC. Due to the cylindrical symmetry of CMS, coordinates in the  $\hat{x}\text{-}\hat{y}$  plane are commonly replaced with the radius  $r$  and the azimuthal angle  $\phi$ , which is measured from the positive  $\hat{x}$ -axis. The polar angle  $\theta$  is measured from the  $+\hat{z}$ -axis, though in practice this variable is rarely used. It is more common to define the polar angle in terms of the pseudorapidity  $\eta$ , which is defined as

$$\eta = \frac{1}{2} \ln \left( \frac{|\mathbf{p}| + p_z}{|\mathbf{p}| - p_z} \right) = -\ln \tan \left( \frac{\theta}{2} \right) \quad (1.4)$$

The motivation for using  $\eta$  instead of  $\theta$  stems from a fundamental property of hadron colliders: the center of mass frame for particle production rarely coincides with the lab frame. Thus, when measuring the separation between particles, it is useful to define quantities that remain invariant under Lorentz transformations in the  $\hat{z}$  direction. The rapidity  $y$  (not to be confused with the Cartesian coordinate  $\hat{y}$ ) is defined as

$$y = \frac{1}{2} \ln \left( \frac{E + p_z}{E - p_z} \right) \quad (1.5)$$

It is trivial to show that differences in  $y$  remain invariant under Lorentz transformations. In the highly relativistic limit, which is valid for most particles produced at the LHC, rapidity approaches pseudorapidity as  $E \approx |\mathbf{p}|$ . One advantage of pseudorapidity is that  $\eta$  can be calculated using only geometric quantities of the detector, whereas  $y$  requires calculating both the energy and momenta of a particle, making pseudorapidity the natural choice for defining the polar angle.  $\eta$  can range from  $(-\infty, \infty)$ , where  $\eta = \pm\infty$  points directly along the  $\pm\hat{z}$  axis. Higher values of  $|\eta|$  are commonly referred to as "forward".

### 1.2.2 Inner Tracker

The CMS inner tracker is the first detector surrounding the primary interaction point (IP). Its purpose is to measure the tracks from charged particles as they curve in the strong magnetic field within CMS in order to calculate their momentum and reconstruct secondary vertices. As the closest detector to the primary IP, the tracker experiences the highest particle flux within CMS, and must have high enough granularity to distinguish the multitude of tracks. Additionally, particles passing through must lose minimal energy in order to maintain their trajectories into the outer detectors. The high flux also makes the detector susceptible to radiation damage, so the tracker must be robust in order to maintain efficiency over the long operational period of the LHC.

The inner tracker utilizes silicon tracking modules to detect the location of charged particles. When an external voltage is applied to a module, particles passing through will deposit energy and create electron-hole pairs, which drift to their respective electrodes and generate an electrical signal. The applied voltage is tuned such that only a small amount of energy is required to produce electron-hole pairs, which reduces the total amount of material required in order to minimize the energy loss of the charged particles. The inner layer of the tracker is composed of higher granularity pixel detectors, while the outer layer is composed of coarser silicon strips.

#### 1.2.2.1 Silicon Pixel Detector

The pixel detector is comprised of 124 million silicon pixel sensors, each with an area of  $100 \times 150 \mu\text{m}^2$  and a thickness of  $300 \mu\text{m}$ . The barrel (BPIX) consists of four cylindrical layers of pixel sensors spanning from  $z = -54 \text{ cm}$  to  $z = 54 \text{ cm}$  at radii of  $r = 2.9, 6.8, 10.9$ , and  $16 \text{ cm}$ . The endcap (FPIX) consists of three layers located at  $z = \pm 29.1, \pm 39.6$ , and  $\pm 51.6 \text{ cm}$ , which when combined with the barrel nets a total sensitive area of  $1.85 \text{ m}^2$  with coverage up to  $|\eta| < 2.5$ . With regards to detector performance, the pixel detector provides

spatial resolution of  $9.5 \mu\text{m}$  in the  $r$ - $\phi$  direction and  $22.2 \mu\text{m}$  in the  $z$  direction, as well as a hit efficiency of  $> 99\%$  in each layer at nominal LHC luminosity, with the innermost BPIX layer dropping to 97.5% at peak run 2 efficiency [3].

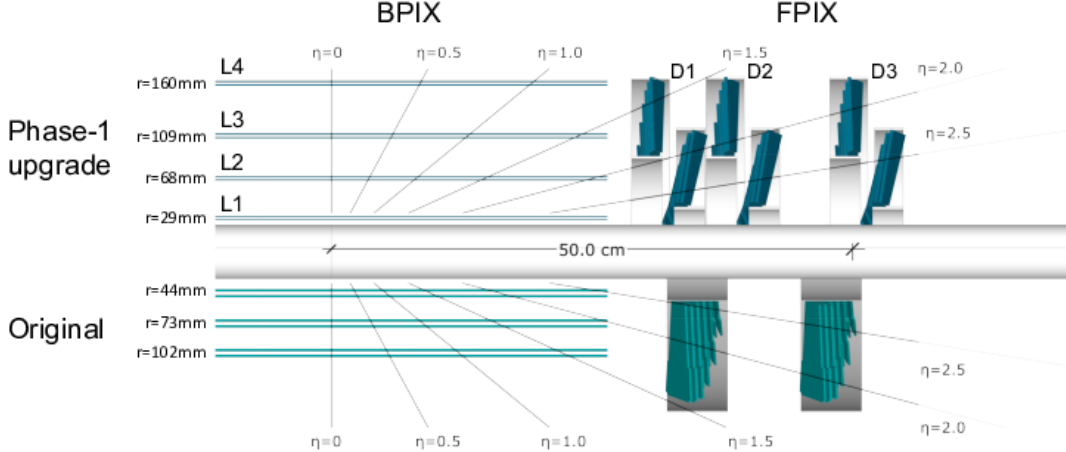


Figure 1.4:  $r$ - $z$  slice of the CMS pixel detector comparing original design (bottom, teal) with the Phase-I upgrade implemented in 2016/17, which added one layer to both the FPIX and BPIX (top, blue) [3].

### 1.2.2.2 Silicon Strip Detector

The silicon strip detector surrounds the pixel detector, and is segmented into a tracker inner barrel (TIB), tracker outer barrel (TOB), tracker inner disks (TID), and tracker endcap (TEC). The TIB consists of four layers covering  $|z| < 65\text{ cm}$  and radius  $25.5\text{ cm} < r < 49.8\text{ cm}$ . The endcaps of the TIB are covered by the TID, consisting of three disks covering  $90 < |z| < 90\text{ cm}$ . Surrounding the TIB is the TOB, with six layers spanning  $|z| < 188\text{ cm}$  and  $60.8 < |r| < 108\text{ cm}$ . Lastly, both the TOB and TID are closed by the TEC, which covers radii ranging from  $22 < r < 113.5\text{ cm}$  and stretches from  $124 < |z| < 280\text{ cm}$ .

The strip detector modules function similarly to the pixel modules, but utilize much larger silicon strips due to the reduced particle flux compared to the pixel detector. Each

strip detector is composed of  $300\ \mu\text{m}$  thick micro-strip sensors with pitch varying from  $80 - 205\ \mu\text{m}$  to form  $7 - 12.5\ \text{cm}$  long strip modules. Overall, the strip detector uses 15,148 modules covering an area of  $200\ \text{m}^2$  up to  $|\eta| < 2.5$ .

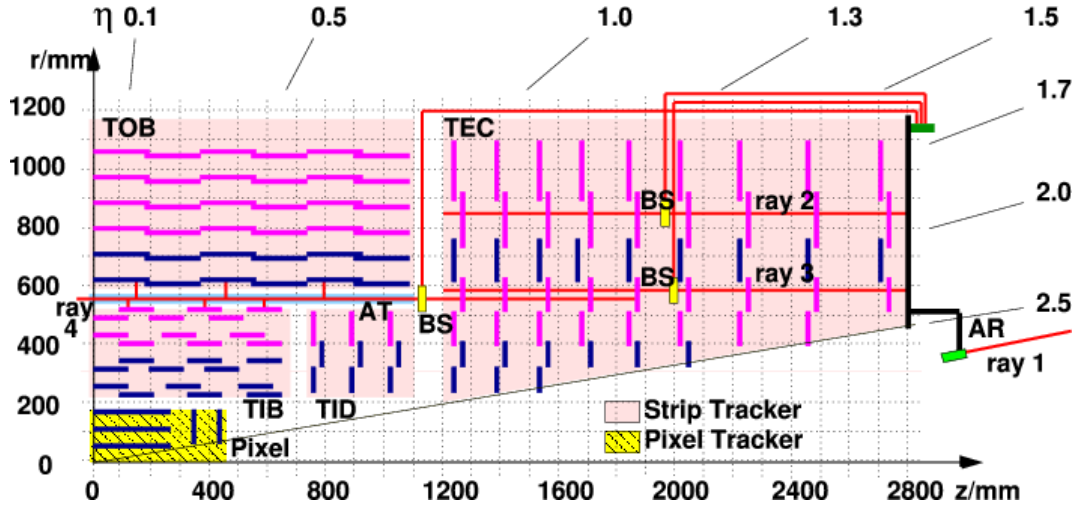


Figure 1.5:  $r$ - $z$  slice of the CMS silicon detector, detailing the four main components (TIB, TOB, TID, and TEC) of the strip detector. Pixel detector is shown in its Run-I configuration [4]

### 1.2.3 Electromagnetic Calorimeter

The CMS Electromagnetic Calorimeter (ECAL) is designed to stop and capture the energy of photons and electrons. When a high energy photon or electron enters the ECAL, it primarily interacts with the material in the detector through  $e^+e^-$  pair production or bremsstrahlung, respectively. These create more photons/electrons that continue this process in a cascade until the particles lose enough energy that ionization and compton scattering begin to dominate. This process is known as an electromagnetic shower. The light produced from a shower is measured using photodetectors to determine the initial energy of the incident photon or electron. The amount of light produced is a poisson process and linearly proportional to the initial energy, so the resolution of the ECAL can be written as

$$\frac{\sigma_E}{E} \propto \frac{1}{\sqrt{E}} \quad (1.6)$$

The material used for an electromagnetic calorimeter can be characterized by the radiation length ( $X_0$ ) and molière radius ( $R_M$ ). The radiation length is the average distance an electron will travel before its energy is reduced by a factor of  $1/e$ , and is roughly proportional to  $A/Z^2$ , where A is the atomic mass and Z is the atomic number. The molière radius is directly proportional to the radiation length and measures the spread of an electromagnetic shower in the transverse direction. Both are generally measured in units of [ $\text{g cm}^{-2}$ ], but can be divided by the density of the material to obtain a distance in [cm]. A low radiation length and molière radius ensure all of the energy is captured in the detector and is contained to a small area to precisely determine the position of an incident particle. It is for this reason that the ECAL is composed of lead-tungstate ( $\text{PbWO}_4$ ): a dense, high Z scintillator crystal with  $X_0 = 7.39 \text{ g/cm}^2$  (or  $0.89 \text{ cm}$  after dividing by the density of  $\text{PbWO}_4$ ) and  $R_M = 2.2 \text{ cm}$  [14].

The ECAL is constructed from  $61200 + 15000$  lead-tungstate crystals in the barrel + endcap region. Barrel crystals have a cross sectional area of  $2.2 \times 2.2 \text{ cm}^2$  to match the molière radius and a depth of  $23 \text{ cm}$  (or  $25.8 X_0$ ), and are arranged in rings along the  $\phi$  direction, tilted to align with lines of constant  $\eta$ . The barrel has an inner radius of  $129 \text{ cm}$  and covers an eta region up to  $|\eta| < 1.479$ . Endcap crystals have a slightly higher cross sectional area of  $2.6 \times 2.6 \text{ cm}^2$  and a slightly lower depth of  $22 \text{ cm}$ , and are arranged in an  $x$ - $y$  grid. The endcap provides the remaining coverage from  $1.479 < |\eta| < 3.0$ . A diagram showing the geometry of the ECAL can be seen in figure 1.6. The size and alignment of the crystals is designed to contain showers from incident photons/electrons within a  $2 \times 2$  grid of crystals.

One common process in CMS is the production of  $\pi^0$ s, which decay to two photons. When the two photons deposit their energy into the ECAL, they can fake a signal from a single high energy photon. In the barrel, the two photons are generally separated by  $\sim 1 \text{ cm}$ ,

so the crystal granularity can be used to distinguish this background from real, high energy photons. However,  $\pi^0$ s in the forward region tend to be higher energy (commonly referred to as "more boosted"), resulting in separations on the order of millimeters. In order to identify these background events, a higher granularity detector known as a preshower is placed before the ECAL endcap. It consists of a layer of lead absorber to initiate the shower, followed by silicon strip sensors to measure the tracks within the shower. The lead has a thickness of 1.57 cm (or  $2.8X_0$ ), thick enough to cause a shower while only causing energy loss of a few percent before the shower can reach the ECAL. The silicon strips are similar to those in the inner tracker, with a pitch of 1.9 mm [15].

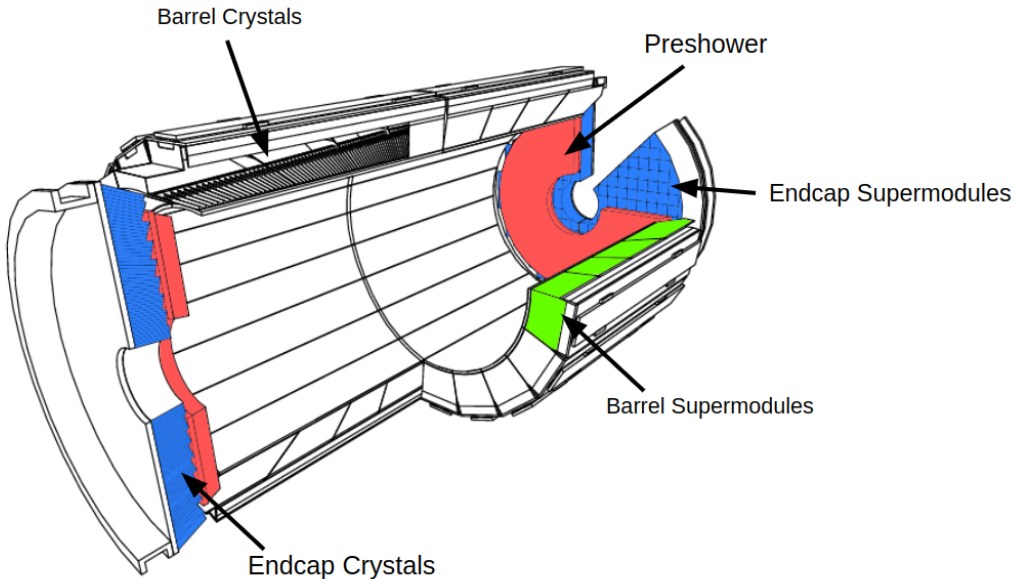


Figure 1.6: Geometry of the CMS ECAL showing the barrel, endcap, and preshower, adapted from [5]

#### 1.2.4 Hadronic Calorimeter

The CMS Hadronic Calorimeter (HCAL) is a sampling calorimeter surrounding the ECAL. Unlike the ECAL, which is a homogeneous calorimeter where the crystals both induce showers

and scintillate, the HCAL is composed of alternating layers of dense absorber and scintillator. The absorber induces hadronic showers - cascades of hadrons resulting from inelastic scattering off a target nuclei. Particles in hadronic showers then pass through the scintillator, which produces light that gets transmitted through wavelength shifting fibers and read out by photodetectors, before repeating this process with the next layer of absorber/scintillator. The measured energy can be summed in sequential layers of detectors (referred to as "towers") to calculate the total energy of the incident hadron. As an additional complication, several hadrons decay to electrons or photons, which will create electromagnetic showers, requiring the scintillator to have good response to electromagnetic interactions. The HCAL must be hermetic, as a complete picture of the energy from proton collisions is required to infer the production of particles like neutrinos, which are otherwise invisible to the detector.

The relevant property for a hadronic absorber is the nuclear interaction length  $\lambda_I$ , which is the mean distance a hadron will travel before undergoing an inelastic nuclear interaction. Like the radiation length,  $\lambda_I$  is measured in [ g cm<sup>-2</sup>] and can be divided by the density to obtain a distance in [ cm]. It is proportional to the density of nuclear matter, which goes as  $A^{1/3}$ . The HCAL uses a combination of brass and stainless steel, both of which have an interaction length of  $\sim 16.5$  cm [16].

The HCAL consists of four subsystems: an inner barrel (HB), an outer barrel (HO), an endcap (HE), and a forward calorimeter (HF). The HB covers  $|\eta| < 1.3$  with 36 azimuthal wedges, each containing 17 layers of alternating brass absorber and scintillator. These wedges begin at a radius of 1.806 m and are 89 cm thick, resulting in a minimum of  $5.3\lambda$  at  $\eta = 0$ , increasing to  $10\lambda$  and  $\eta = 1.2$ . The HE consists of two disks, also formed of 36 wedges with 19 layers of brass absorber and scintillator, totaling  $10\lambda_I$  in order to contain highly boosted, forward jets. The HE extends the coverage of the HCAL up to  $|\eta| < 3.0$ . The HO is located outside the magnetic coil to catch high energy ( $> 100$  GeV) hadrons that escape the HB. It consists of five rings in eta, covering up to  $|\eta| < 1.2$ , and relies on the iron solenoid to induce hadronic showers. The HF covers the most forward region of  $3 < |\eta| < 5$ . This

zone has the highest exposure of radiation, and so the detector must be sensitive only to the highest energy particles and robust against damage from heavy radiation. It uses steel as the absorber and quartz fibers to scintillate through Cherenkov radiation. The four subsystems provides a minimum of  $10\lambda$  to capture incident hadrons.

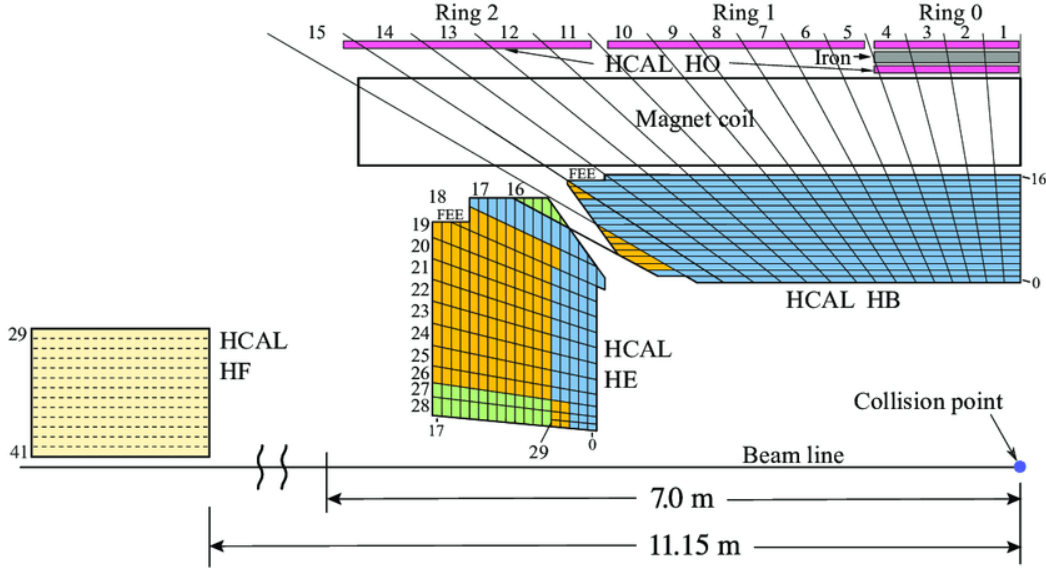


Figure 1.7:  $r$ - $z$  slice of the CMS HCAL showing the HB, HE, HF, and HO [6]

### 1.2.5 Muon Detectors

The muon chambers lie outside the magnetic solenoid as the outermost subsystem in CMS. Due to the distance and amount of material between them and the primary IP, they are the lowest occupancy detectors, with few particles other than muons able to reach them before decaying or stopping in the inner subsystems. Although they lie outside the solenoid, the iron yolk pulls the magnetic field back, curving the trajectory of muons, which is required calculate their momenta. The detector subsystem is composed of three types of gaseous detection chambers: drift tubes (DTs), resistive plate chambers (RPCs), and cathode strip chambers (CSCs). A diagram showing the configuration of these detection chambers can be seen in figure 1.8.

The operating physics principles of all three chambers are similar: muons pass through a gas mixture and ionize the gas, knocking loose electrons. Anodes and cathodes create an electric field inside the gas chamber, causing the electrons to drift to the anode where they can be measured and read out by electronics. Electrons that are excited but not ionized from the incident muon will emit photons as they transition back to a lower energy level, thus a quenching gas is used to absorb these photons to prevent further cascades. The specifics of the three detectors are described in sections 1.2.5.1-1.2.5.3.

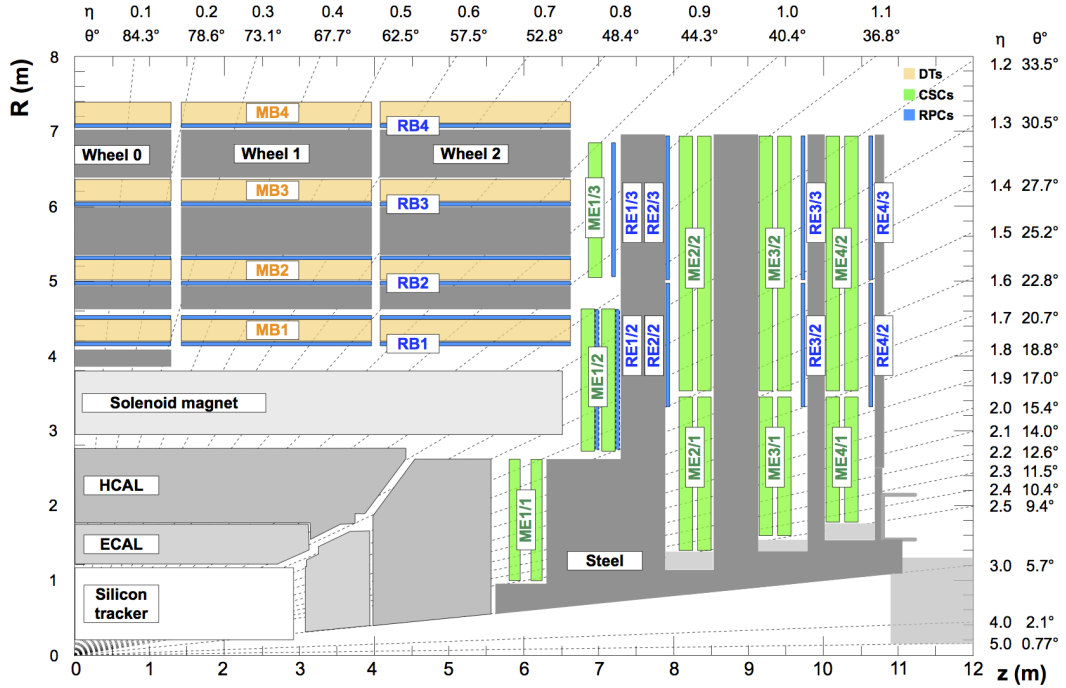


Figure 1.8:  $r$ - $z$  cross section of the CMS muon detector subsystem, configured for the 2016-2018 data taking run. The barrel consists of five wheels of DTs and RPCs in  $\eta$ , each wheel consisting of four layers in  $r$  and 12 sectors in  $\phi$ , covering up to  $|\eta| < 1.2$ . The endcap consists of four layers of DTs and RPCs in  $z$  [7]

### 1.2.5.1 Drift Tubes

Drift tubes are used in the barrel of the muon system, covering  $|\eta| < 1.2$ . They consist of long chambers filled with an mixture of AR/CO<sub>2</sub>, with an anode wire running lengthwise through the center and cathode strips along the edges. Electrode strips along the outer edge of the chamber shape the electric field lines to linearize the drift velocity of electrons throughout the chamber. When a muon passes through the chamber, ionized electrons follow the electric field lines towards the anode wire. Due to the known field inside the chamber, the drift time can be used to calculate the transverse distance from the wire to the incident muon with a resolution of 250  $\mu\text{m}$ . The DTs are arranged in superlayers, which consist of 4 layers of DTs, with subsequent superlayers alternating in the  $r$ - $z$  and  $r$ - $\phi$  direction in order to obtain the muon trajectory/curvature in both the  $\eta$  and  $\phi$  direction. Figure 1.9 shows a diagram of a DT superlayer and a single DT cell.

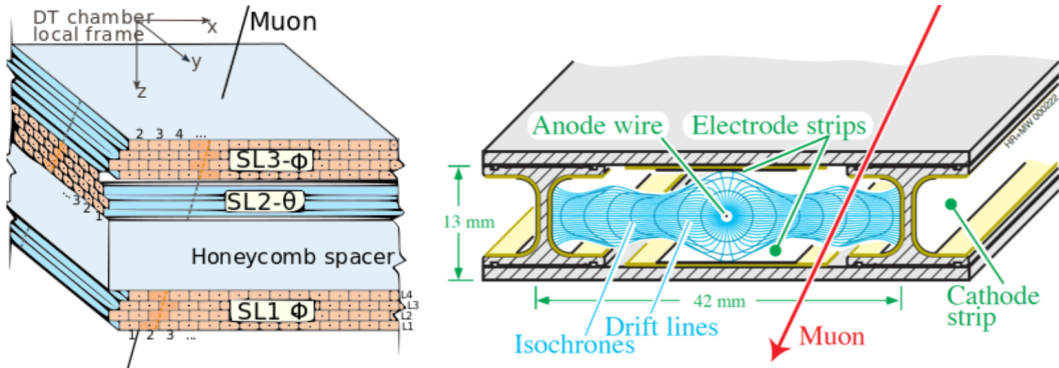


Figure 1.9: Drift tube superlayers are aligned in alternating orientations in order to provide a complete picture of muon trajectories (left). A cross section of a single drift tube chamber (right). Electrons ionized from the muon drift to the anode wire to produce a measurable current [8]

### 1.2.5.2 Cathode Strip Chambers

Cathode strip chambers are used in the endcaps of the muon system to provide coverage from  $0.9 < |\eta| < 2.4$ . CSC modules are trapezoidal chambers filled with a mixture of Ar/CO<sub>2</sub>/CF<sub>4</sub> and arranged in disks to cover the muon endcap. Each module is composed of six layers of radial cathode strips, which have high granularity in  $\phi$ , and transverse anode wires which provide granularity in  $r$ . Similar to the DTs, muons passing through CSC chambers ionize the gas molecules, knocking loose electrons which drift to the anode wires. The charge from these electrons can be measured and provides the position of the muon in  $r$ . Simultaneously, the electrons induce a charge in the cathode strips, which provides the position of the muon in  $\phi$ . One chamber provides a spatial resolution of between 40–50  $\mu\text{m}$  with a time resolution of 3 ns.

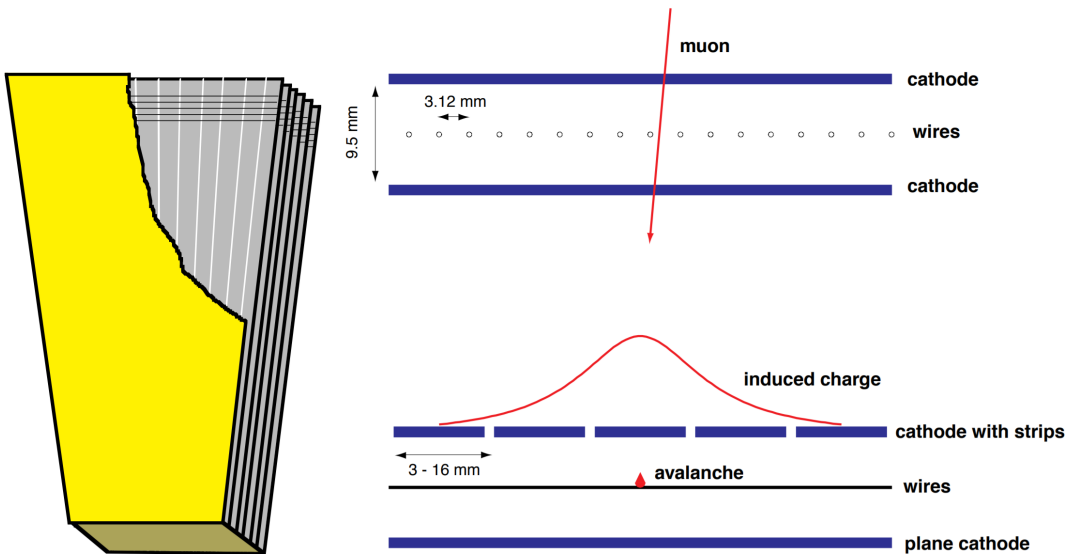


Figure 1.10: Cut-away diagram of a single CSC module showing the six layers of radial cathode strips and transverse anode wires (left). Muons ionize the gas chamber, causing an avalanche of electrons on the anode wires and inducing a charge on the cathode strips (right) [9]

### 1.2.5.3 Resistive Plate Chambers

RPC detectors are used in conjunction with the DTs and CSCs in both the barrel and endcap. One RCP consists of two high resistivity plastic plates: one positively charged anode and a negatively charged cathode which create a strong, uniform electric field between the two. The space between the two plates is filled with a mixture of 95%  $\text{C}_2\text{H}_2\text{F}_4$  and 5% iso- $\text{C}_4\text{H}_{10}$ . Incident muons ionize the gas between the two plates, which cause a cascade of electrons towards the anode plate due to the strong electric field. External metal strips lie outside the anode in order to measure the avalanche of electrons. The coarse nature of the strips means the RPC spatial resolution is lower than that of the CSCs and DTs at around 1 cm, but the time resolution is much faster at  $\sim 1$  ns. For this reason they are used to supplement the CSC and DTs to aid with triggering and accurate timing.

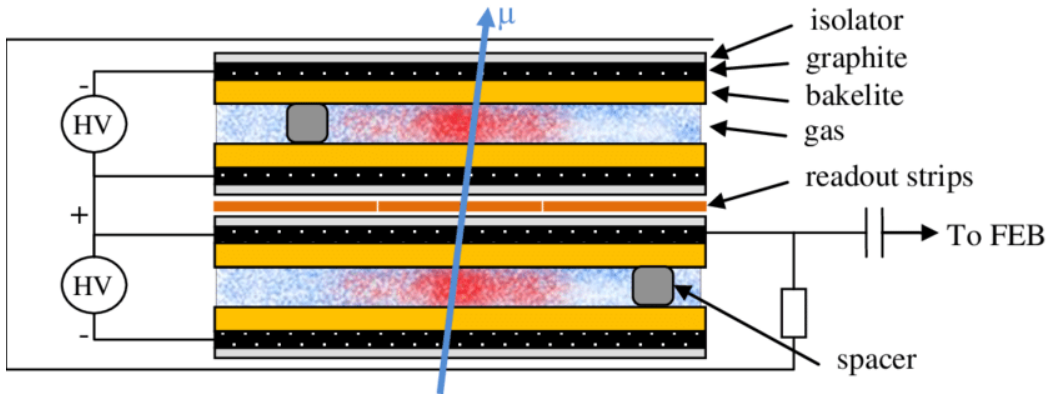


Figure 1.11: Diagram of the double RPC at CMS. Incident muons ionize the gas, causing a cascade of electrons towards the readout strips [10]

### 1.2.6 Trigger System

The high luminosity of the LHC yields an incredibly high rate of information to store from the various detectors. Each event contains approximately 1 MB of data to store, which would take bandwidth and storage space beyond current capacities to save given the 40 MHz

collision rate. Additionally, many events do not contain interesting physics worth storing for further analysis. In order to reduce the rate of events and filter uninteresting collisions, CMS employs a two level trigger system. The first level is known as the Level-1 (L1) trigger and uses hardware to identify physics objects in real time. The second is known as the High-Level trigger (HLT), consisting of a conventional CPU farm which performs more advanced calculations.

#### 1.2.6.1 Level-1 Trigger

The L1 trigger utilizes special processors such as Field Programmable Gate Arrays (FPGAs) in order to process coarse information from the calorimeters and muon chambers in real time. The coarse detector information, known as trigger primitives, is subjected to several algorithms to create physics objects (e.g. muons, electrons, etc). Objects passing a predetermined set of criteria are called trigger "seeds", with events that satisfy at least one seed getting passed to the HLT. A diagram of the L1 trigger architecture can be seen in figure 1.12. This entire decision making process must take place in  $3.2 \mu\text{s}$  after a bunch crossing. As this is greater than the time between bunch crossings, the L1 trigger must be pipelined in order to operate continuously, while the full data is kept in a rolling buffer and read out only if the event passes a trigger seed. The L1 trigger was designed to accept events at a maximum rate of 100 kHz, meaning only one in every four hundred events is passed to the HLT.

#### 1.2.6.2 High Level Trigger

The HLT receives the full precision detector data for events passing the L1 trigger, and is designed to reduce the final event rate to 100 Hz, five orders of magnitude less than the LHC bunch crossing rate. Information from the tracker allows the HLT algorithms to reconstruct a more complete picture of an event, as tracker information can be matched to

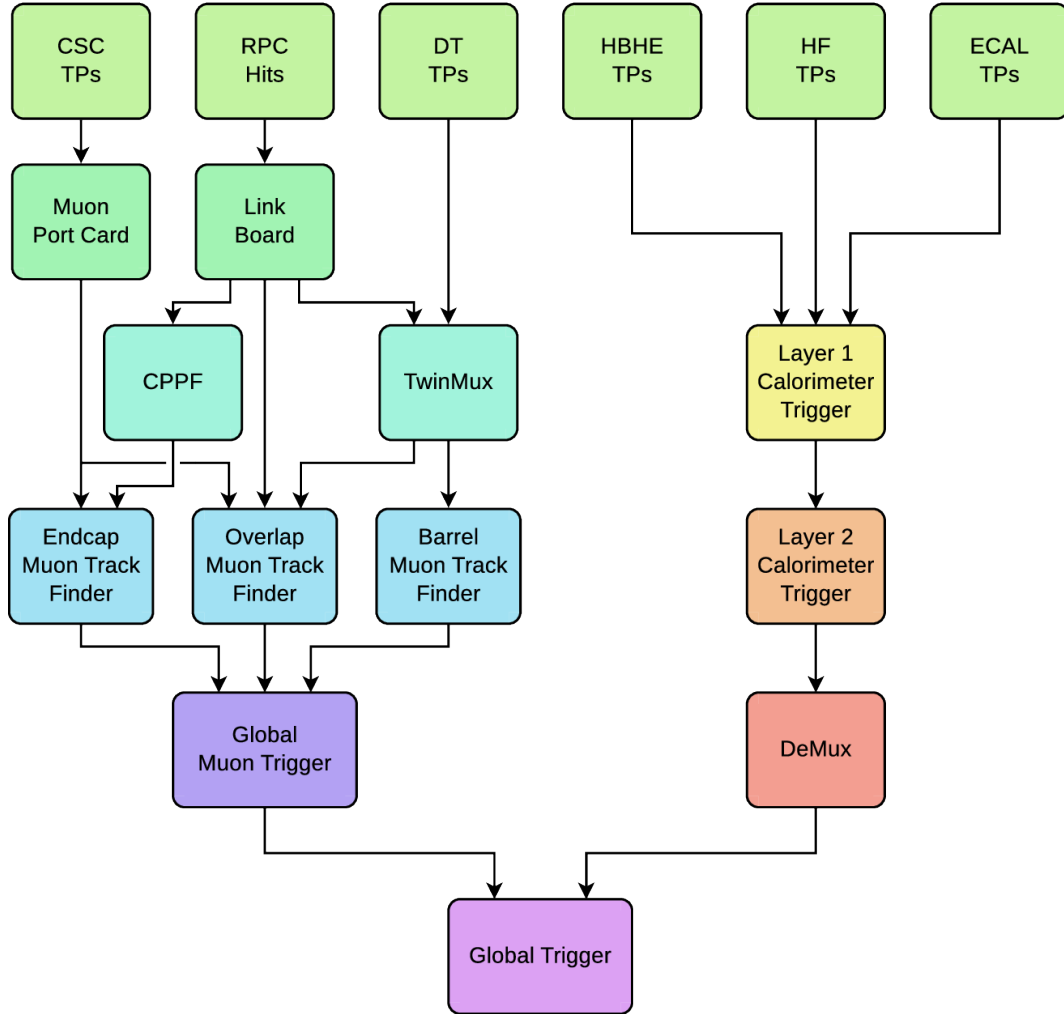


Figure 1.12: Block diagram of the CMS Level-1 Trigger architecture during Run 2 [11]. Muon objects found in the barrel, overlap, and endcap regions are ranked and sorted using their momentum and quality criteria before being passed to the Global Muon Trigger (GMT), which cleans duplicate tracks and selects the top eight muons. The muons are then passed to the global trigger, which combines the muons with objects created from the calorimeters and makes the final decision to pass the event to the HLT.

both calorimeter hits and muon tracks provide more detail to reconstructed physics objects. As with the L1 trigger, the HLT processes data through a series of trigger paths, which sequentially reconstruct and filter physics objects. In order to optimize computation time, the HLT uses L1 trigger seed to inform which trigger paths to use, and structures the paths in order to increasing complexity. Events passing the HLT are then recorded permanently for offline reconstruction and analysis.

## REFERENCES

- [1] CMS Collaboration. CMS luminosity - public results, 2018. URL: <https://twiki.cern.ch/twiki/bin/view/CMSPublic/LumiPublicResults>.
- [2] Tai Sakuma. Cutaway diagrams of CMS detector. 2019. URL: <http://cds.cern.ch/record/2665537>.
- [3] The Tracker Group Of The CMS Collaboration. The cms phase-1 pixel detector upgrade, 2020. URL: <https://arxiv.org/abs/2012.14304>, doi:10.48550/ARXIV.2012.14304.
- [4] S Chatrchyan et al. Alignment of the CMS silicon tracker during commissioning with cosmic rays. *JINST*, 5:T03009, 2010. URL: <https://cds.cern.ch/record/1211825>, arXiv:0910.2505, doi:10.1088/1748-0221/5/03/T03009.
- [5] Badder Marzocchi. Simulation of the cms electromagnetic calorimeter response at the energy and intensity frontier. *Journal of Physics: Conference Series*, 1162:012007, 01 2019. doi:10.1088/1742-6596/1162/1/012007.
- [6] Albert M Sirunyan et al. Calibration of the CMS hadron calorimeters using proton-proton collision data at  $\sqrt{s} = 13$  TeV. *JINST*, 15:P05002, 2020. Replaced with the published version. Added the journal reference and the DOI. All the figures and tables can be found at <http://cms-results.web.cern.ch/cms-results/public-results/publications/PRF-18-001> (CMS Public Pages). URL: <https://cds.cern.ch/record/2691403>, arXiv:1910.00079, doi:10.1088/1748-0221/15/05/P05002.
- [7] A.M. Sirunyan et al. Performance of the CMS muon detector and muon reconstruction with proton-proton collisions at  $\sqrt{s} = 13$  TeV. *JINST*, 13(06):P06015, 2018. Replaced with the published version. Added the journal reference and the DOI. All the figures and tables can be found at <http://cms-results.web.cern.ch/cms-results/public-results/publications/MUO-16-001> (CMS Public Pages). URL: <http://cds.cern.ch/record/2313130>, arXiv:1804.04528, doi:10.1088/1748-0221/13/06/P06015.
- [8] CMS Collaboration. Muon drift tubes. URL: <https://cms.cern/detector/detecting-muons/muon-drift-tubes>.
- [9] Isabelle Helena J De Bruyn. Electronics upgrade for the CMS CSC muon system at the High Luminosity LHC. Technical report, CERN, Geneva, 2019. URL: <http://cds.cern.ch/record/2797803>.
- [10] Priyanka Kumari. Improved-rpc for the cms muon system upgrade for the hl-lhc, 2020. URL: <https://arxiv.org/abs/2005.11396>, doi:10.48550/ARXIV.2005.11396.

- [11] Albert M Sirunyan et al. Performance of the CMS Level-1 trigger in proton-proton collisions at  $\sqrt{s} = 13$  TeV. *JINST*, 15(10):P10017, 2020. Replaced with the published version. Added the journal reference and the DOI. All the figures and tables can be found at <http://cms-results.web.cern.ch/cms-results/public-results/publications/TRG-17-001> (CMS Public Pages). URL: <https://cds.cern.ch/record/2721198>, arXiv: 2006.10165, doi:10.1088/1748-0221/15/10/P10017.
- [12] Oliver Sim Brüning, Paul Collier, P Lebrun, Stephen Myers, Ranko Ostojic, John Poole, and Paul Proudlock. *LHC Design Report*. CERN Yellow Reports: Monographs. CERN, Geneva, 2004. URL: <https://cds.cern.ch/record/782076>, doi: 10.5170/CERN-2004-003-V-1.
- [13] Esma Mobs. The CERN accelerator complex - august 2018. complexe des accélérateurs du CERN - août 2018. Aug 2018. General Photo. URL: <https://cds.cern.ch/record/2636343>.
- [14] R. L. Workman and Others. Review of Particle Physics. *PTEP*, 2022:083C01, 2022. doi:10.1093/ptep/ptac097.
- [15] E. Tournefier. The preshower detector of cms at lhc. *Nuclear Instruments and Methods in Physics Research Section A: Accelerators, Spectrometers, Detectors and Associated Equipment*, 461(1):355–360, 2001. 8th Pisa Meeting on Advanced Detectors. URL: <https://www.sciencedirect.com/science/article/pii/S0168900200012432>, doi: [https://doi.org/10.1016/S0168-9002\(00\)01243-2](https://doi.org/10.1016/S0168-9002(00)01243-2).
- [16] G Baiatian et al. Design, Performance, and Calibration of CMS Hadron-Barrel Calorimeter Wedges. Technical Report 1, CERN, Geneva, 2008. URL: <http://cds.cern.ch/record/1049915>, doi:10.1140/epjc/s10052-008-0573-y.